

2 Planar Pixel Sensors for the ATLAS Upgrade: Beam 3 Tests results

J. Weingarten^{1,*}, S. Altenheiner², M. Beimforde³, M. Benoit⁴, M. Bomben⁵, G. Calderini^{5,6}, C. Gallrapp⁴, M. George¹, S. Gibson⁴, S. Grinstein⁷, Z. Janoska⁸, J. Jentsch⁴, O. Jinnouchi⁹, T. Kishida⁹, A. La Rosa¹⁰, V. Libov¹¹, A. Macchiolo³, G. Marchiori⁵, D. Münstermann⁴, R. Nagai⁹, G. Piacquadio⁴, B. Ristic², I. Rubinskiy¹¹, A. Rummler², Y. Takubo¹², G. Troska², S. Tsiskaridze⁷, I. Tsurin¹³, Y. Unno¹², P. Weigell³, T. Wittig²

¹*II. Physikalisches Institut, Georg-August-Universität Göttingen, Germany*

Email: jens.weingarten@uni-goettingen.de

²*Technische Universität Dortmund, Fakultät Physik, Dortmund, Germany*

³*Max-Planck-Institut für Physik, München, Germany*

⁴*CERN, Genève, Switzerland*

⁵*Laboratoire de Physique Nucleaire et de Hautes Énergies (LPNHE), Paris, France*

⁶*Dipartimento di Fisica E. Fermi, Università di Pisa, and INFN Sez. di Pisa, Pisa, Italy*

⁷*Institut de Física d'Altes Energies (IFAE), Bellaterra, Spain*

⁸*Division of elementary particle physics - Institute of Physics of the Academy of Sciences of the Czech Republic, Prague, Czech Republic*

⁹*Tokyo Institute Of Technology, Tokyo, Japan*

¹⁰*Section de Physique (DPNC), Université de Genève, Genève, Switzerland*

¹¹*Deutsches Elektronen-Synchrotron (DESY), Hamburg, Germany*

¹²*High Energy Accelerator Research Organization, Tsukuba, Japan*

¹³*The University of Liverpool, Liverpool, United Kingdom*

4

ABSTRACT: Results of beam tests with planar silicon pixel sensors aimed towards the ATLAS Insertable B-Layer and High Luminosity LHC (HL-LHC) upgrades are presented. Measurements include spatial resolution, charge collection performance and charge sharing between neighbouring cells as a function of track incidence angle for different bulk materials.

5 Measurements of n-in-n pixel sensors are presented as a function of fluence for different irradiations. Furthermore p-type silicon sensors from several vendors with slightly differing layouts were tested. All tested sensors were connected by bump-bonding to the ATLAS Pixel read-out chip. We show that both n-type and p-type tested planar sensors are able to collect significant charge even after integrated fluences expected at HL-LHC.

6 **KEYWORDS:** Silicon pixel detectors, planar sensors, radiation damage to detector materials (solid
7 state), beam tests, simulations, ATLAS upgrade, HL-LHC, SLHC.

*Corresponding author.

9 Contents

10	1. Introduction	1
11	2. Beam test setup	2
12	2.1 The EUDET telescope	3
13	2.2 Devices Under Test	3
14	3. The beam test analysis	4
15	3.1 Track reconstruction	4
16	3.2 Detector alignment	4
17	3.3 Data analysis	5
18	3.3.1 Description of tbmon analyses	5
19	4. The n-in-p demonstrator program	6
20	4.1 CiS sensors	6
21	4.1.1 Sensor design	6
22	4.1.2 Beam test results	7
23	4.2 HPK sensors	11
24	4.2.1 Sensors design	11
25	4.2.2 Beam test results	13
26	5. Radiation hardness of n-in-n sensors	15
27	5.1 Results	17
28	6. Slim Edge	20
29	7. Conclusion	22

31 1. Introduction

32 The ATLAS collaboration will upgrade the current Pixel Detector [1] in the next 10-15 years in
 33 two phases. A first upgrade will be realized during the shut-down in 2013, by inserting a fourth
 34 detection layer (Insertable B-Layer - IBL) at a radius of 3.2 cm from the interaction point. The IBL
 35 will improve the tracking and vertexing performance of the current pixel detector significantly,
 36 while the LHC will take data at its nominal centre-of-mass energy ($\sqrt{s} = 14$ TeV) [2].

37 The short distance from the interaction point places the IBL in a very harsh environment in
 38 terms of radiation damage. Until the end of operation (foreseen around 2020) the IBL will have to
 39 sustain an estimated fluence, including safety factors, of 5×10^{15} n_{eq}/cm² (which corresponds to a
 40 60% safety factor at $r = 3.2$ cm).

The final luminosity upgrade for the LHC (beyond 2020) foresees a factor of 5-10 more in peak luminosity, posing serious constraints on the technology for the ATLAS tracker in the High Luminosity era (HL-LHC): the estimated fluence, including safety factors, for the innermost layer will be on the order of $2 \times 10^{16} \text{ n}_{eq}/\text{cm}^2$ [3] after 7 years of High-Luminosity runs. Hence, in view of a possible pixel system replacement after 2020, new pixel sensors are under study.

Different sensor options are being developed in parallel to address the challenges imposed by the foreseen luminosity upgrades. They include diamond sensors [5] and 3D silicon sensors, with implants going through the sensor bulk [6]. Within the Planar Pixel Sensor project (PPS) [7] several optimizations of this well-known technology, aiming towards the different planned upgrades of the ATLAS detector, are under investigation.

The PPS project investigates the suitability of different materials (p- and n-bulk, diffusion oxygenated float zone, magnetic Czochralski) and different geometries (slim edge design, number and width of guard rings) for a new generation of planar pixel sensors. First prototypes have been subject of several tests in order to assess the performance of the new sensors. Among the various tests, new detectors were brought to beam tests in 2010 for the first time. In this paper we will present the beam test results in three different areas of our scientific program: the n-in-p demonstrator program, the n-bulk radiation-hardness studies and the “slim edge” proof-of-concept.

The paper is organized as follows. After having illustrated the experimental setup of the beam tests (Section 2), and some details of the data analysis (Section 3) we will introduce the n-in-p demonstrator program (Section 4): several p-bulk detectors that were tested in 2010 will be described; n-in-p detectors’ performance, such as collected charge, charge sharing probability and spatial resolution, will be presented and discussed.

In Section 5 the n-bulk radiation-hardness will be studied, based on the beam test results. We will show that n-in-n detectors are operable after an integrated fluence comparable to that expected for IBL ($5 \times 10^{15} \text{ n}_{eq}/\text{cm}^2$) and at the foreseen nominal bias voltage for the future 4th ATLAS Pixel layer. Noise occupancy, charge collection performance, charge sharing probability and spatial resolution will be presented.

The new pixel sensors will not only have to sustain the harsher environment, but also have to show high geometrical acceptance without overlapping adjacent modules: the future material budget restrictions and the geometrical limitations ask for a geometry inefficiency below 2.5%. Hence the inactive areas of the future pixel sensor should be less than $450 \mu\text{m}$ wide [2]. For this reason, efforts were devoted to design detectors with reduced dead area. The “slim edge” detector-concept will be presented in Section 6, together with its performance in terms of charge collection at the detectors’ edge.

2. Beam test setup

Beam tests are crucial for characterizing the performance of any particle detector. Planar silicon sensors for the ATLAS upgrade have been tested in several beam tests in 2009 and 2010. Data presented in this paper was taken in two different periods in 2010 at the CERN SPS beamline H6. In both periods pion beams of $120 \text{ GeV}/c$ were used. The high momentum of the beam particles minimizes the influence of multiple scattering, allowing for high precision tracking of the beam particles using the EUDET beam telescope [8].

2.1 The EUDET telescope

The telescope consists of six equal planes, divided into two groups (arms) of three planes each. The Devices Under Test (DUTs) were mounted in between these two arms of the telescope as well as downstream of the last telescope plane. The increase of the track extrapolation error downstream of the telescope was minimized by mounting the DUTs as close as possible to the last telescope plane.

The sensitive elements of the telescope planes are Mimosa26 [25] active pixel sensors with a pixel pitch of $18.4\,\mu\text{m}$. Each plane consists of 1152×576 pixels covering an active area of $21.2 \times 10.6\,\text{mm}^2$. The tracking resolution between the telescope arms is estimated to be $2\,\mu\text{m}$, at the position of the samples downstream of the telescope it is on the order of $10\,\mu\text{m}$. [26]

A coincidence of four scintillators (two upstream and two downstream of the telescope) was used for triggering, which resulted in an effective sensitive area of $2 \times 1\,\text{cm}^2$.

2.2 Devices Under Test

All DUTs were read out using the current ATLAS Pixel readout chip (FE-I3) [9]. The FE-I3 chip is an array of 160 rows \times 18 columns of $50\,\mu\text{m} \times 400\,\mu\text{m}$ read-out cells. In each readout cell the sensor charge signal is amplified and compared to a programmable threshold by a discriminator. The information on the collected signal is encoded through a digital time over threshold (ToT) [9] measured in units of 25 ns, which is the LHC bunch crossing rate. ToT to charge conversion has been tuned for each individual pixel to 60 ToT for a deposited charge of 20 ke. Discriminator thresholds were tuned to a charge of 3.2 ke. Tuning was performed for every readout chip in conditions as close as possible to the beam test ones before testing them in the beam. Since especially the ToT-tuning is very temperature dependent, a calibration of the ToT has been performed on each sample after installation in the beam test setup to give a proper charge conversion. The data were collected using the PC-VME based TurboDAQ system [10]. For enabling a synchronous readout of the TurboDAQ system with the EUDET telescope several extensions were needed. These were summed up in [17].

For each DUT a fiducial region was defined; the selection was based on geometrical and operability parameters. For most studies only the performance of central pixels is of interest. Therefore in many analyses the pixels at the edges of the sensors were masked. Beside that, all pixels that were found to have disconnected or merged bump-bonds in laboratory measurements were masked. Pixels with high noise occupancy are masked.

Devices were irradiated to different fluences using 25 MeV energy protons at the Irradiation Center in Karlsruhe [19], 24 GeV/c momentum protons at the IRRAD-1 CERN Irradiation facility [12], and reactor neutrons at the TRIGA reactor of the Jožef Stefan Institute, Ljubljana [18]. The radiation damage from the different irradiations is scaled to the equivalent damage from 1 MeV neutrons using the NIEL hypothesis [30]. During the irradiations the devices were not powered and not cooled. No standard annealing procedure was used, but samples were stored below $0\,^{\circ}\text{C}$ to avoid uncontrolled annealing.

For the beam tests, irradiated DUTs were cooled through a strip of copper tape thermally connecting the backside of the DUTs with the base plate of the thermal enclosure. The base plate was in

turn cooled using dry ice (CO₂) [17]. The operation temperature was kept all the time in the range between -45 and -15 °C.

3. The beam test analysis

3.1 Track reconstruction

The track reconstruction is realized in consecutive steps. In a first step the raw data, containing the hits of all telescope planes and DUTs, are converted into the EUTelescope [23] internal data format for further treatment. During this process, the time stamp of every hit is checked against the unique time stamp of the event provided by the Trigger Logic Unit (TLU) [24] and, in case synchronization was lost, the hit is resynchronized to its corresponding event. In this context an event is defined as hits from all planes belonging to one trigger. When receiving a trigger signal, the telescope planes and DUTs are being read out. Due to the rolling shutter read-out of the Mimosa26 sensors, it takes 112 μ s to read the full frame. This is much longer than the 400 ns hit-buffer of the DUTs, so some tracks will be recorded by the telescope, but not by the DUTs. In order to estimate if a hit is expected, a matched reference hit in one of the other DUTs is required. This ensures that all tracks used for the measurements are within the DUT's timing window. A clustering algorithm is then executed searching for clusters in all planes. Exploiting the geometry description of the whole setup, hits are transformed from local coordinates to a global coordinate system, which has the z-axis along the beam-direction, y-axis along the vertical direction and the x-axis is then defined to have a right-handed Cartesian coordinate system. During this coordinate transformation rotations of the DUTs along all axes, pixel sizes in x- and y-direction and the specified z-position of all sensors are taken into account. Based on the hit positions in the global frame, a coarse pre-alignment is calculated. Using this information, the final alignment processor (see also 3.2) tries to fit tracks through all planes in the setup, taking into account the different pointing resolutions of the planes and individual track selection criteria for each plane. The final step is the track-fitting, which is based on a Kalman filter [29]. Unbiased tracks are fitted, requiring a hit in at least four out of the six telescope planes and in at least one DUT. Also in this step, different track selection criteria can be applied. The parameters of all reconstructed tracks are finally stored into a ROOT file [31], which can be further analysed (see Section 3.3).

3.2 Detector alignment

The alignment for the telescope planes and the DUTs in the EUTelescope track-reconstruction uses the MILLPEDE tool [27]. In the algorithm the alignment constants are calculated such that the uncertainties of the fitted track parameters, as well as the χ^2 of the tracks, are minimized. In the process, straight lines are fitted through the hit positions of all active planes. This process takes place independently for the x and y directions. For the resulting residual distributions, individual criteria can be applied to suppress fake tracks. Individual selection criteria are especially necessary, since the pixel size of the telescope-planes is 18.4 μ m in both directions, whereas the investigated FE-I3 based samples have a pixel size of 400 μ m x 50 μ m. In the whole alignment process the pre-alignment constants, calculated in the previous hitmaker step based on sensors hit-position correlations, are taken into account. Using pre-alignment gives the possibility to align all

telescope-planes and DUTs in one step, where just the first telescope-plane is fixed in its position and orientation. Finally MILLIPEDE returns a set of x and y translations, as well as rotations for each plane. This information is applied in the final track fitting process.

3.3 Data analysis

The analysis of the reconstructed tracks is conducted in several steps, using a data analysis framework (tbmon) [28].

First, unresponsive (“dead”) and noisy pixels are identified and masked. A pixel is dead if it did not register any hit over a full data taking period and noisy if more than 5×10^{-4} of all hits registered in this pixel are out of time. Less than 1 % of pixels were masked in non-irradiated modules; for irradiated devices the fraction was significantly different for each assembly, however always below 30 %, and on average roughly 10 %.

For the pixel which passed this first selection the alignment is checked per run. The mean positions of the residuals are used to correct the DUT positions on a per run basis. In the next step the η -correction factors [13] are determined. Using these corrections, the alignment is checked a second time.

For the following analyses a track has to fulfill several quality criteria, as cuts on the χ^2 determined from the track fitting and checks on the fiducial region of the sensor.

Tracks extrapolated from the telescope are “matched” to a hit if the hit and the extrapolated track impact point in the DUT plane containing the hit are closer than 400 μm in the long pixel direction and 150 μm in the short pixel direction

3.3.1 Description of tbmon analyses

In the following subsection the individual tbmon analyses are introduced.

Cluster size Clustering is performed using a simple algorithm that starts from an active pixel and adds its neighboring pixels to the cluster if they contain a hit. Along the long pixel direction, only direct neighbors are considered, while along the short pixel direction an active pixel is added to the cluster even if one pixel in between does not show a hit. This allows for the possibility of split clusters. The cluster size is defined as the number of active pixels forming a cluster.

Residuals To estimate the intrinsic spatial resolution of the DUTs the distribution of hit residuals has been studied for each sensor in different configurations. The hit residual is defined as the difference between the reconstructed hit position on the DUT and the extrapolation of the fitted track to the DUT plane. The hit position is defined as the η corrected ToT weighted position of the different pixels in the cluster [13].

Using the residual distributions for all clusters the intrinsic spatial resolution has been estimated by the RMS of the distribution. The residual distribution of 2-pixel clusters is fitted with a sum of two Gaussian functions, a “core” and an “outlier” one. The outlier Gaussian represents mis-reconstructed hits, resulting in large residual values (equal to 2 times the pixel pitch or more), while its mean fixed at zero; the core Gaussian includes correctly reconstructed hits. The width of the core Gaussian gives the width of the region in which charge sharing occurs between neighboring pixels [14].

Collected charge The pulse height is obtained by the ToT technique and transformed into a charge value based on a calibration taken for each pixel of a cluster within the beam test setup. If this information is combined with the tracking information a position resolved charge collection profile of the sensor, referred to as sub pixel resolved charge collection profile, can be obtained. This allows the study of pixel layout features, *e.g.* the bias grid region on the right side of the plot [15].

2D charge sharing To determine the charge sharing probability for each hit within a cluster, it is determined if a hit is found in a pixel cell adjacent to the one matched to a track. This probability rises towards the edge of the pixel since in this region the charge carriers are more likely to drift to the neighbouring pixel. The resulting map is centred on one pixel and in each direction half of the adjacent pixel is shown. The increased probability of charge sharing can be seen along the edges and in the four corners. On the side where the bias grid is located the charge sharing probability is reduced; this will be discussed along with the results. The overall charge sharing is defined by the number of tracks where at least one hit was found in a neighbouring pixel divided by the number of all tracks.

4. The n-in-p demonstrator program

While n-type bulk sensors require patterned guard rings on the back side of the sensor, for p-type material these can be moved to the pixellated side of the sensor (front side); then metallization is the only process for the back side. This makes it a very cost-effective material for future pixel detectors. On the other hand the high voltage, which is applied to the back side of the sensor, is also present on the edges of the front side of the sensor facing the read-out chip, which is at ground potential. Thus spark discharges may happen, posing a risk to the readout electronics itself. This can be limited by the deposition of an insulating coating on the edge of the sensor; more details will be given in the next section.

Sensors in p-type technology tested in 2010 were produced at CiS¹ and at HPK². In Table 1 an overview of all relevant quantities for the studied devices in the beam test is given. In the following each sample is described.

4.1 CiS sensors

In the following the p-type sensors produced at CiS will be introduced and their beam test results discussed.

4.1.1 Sensor design

The n-in-p pixel sensors labelled as MPP1–MPP5 have been produced at CiS with a geometry compatible with FE-I3, in the framework of a common RD50 production [20]. Two different guard-rings structures, with different widths, have been implemented, with one of them characterized by a reduced non-active area (Figure 1) with respect to the 1 mm per side of the ATLAS pixel sensors. MPP1, MPP3 and MPP5 have 19 guard-rings, with the standard total inactive width of 1 mm on

¹Forschungsinstitut für Mikrosensorik und Photovoltaik GmbH

²Hamamatsu Photonics K. K.

sample	Period	fluence ($10^{15} \text{ n}_{eq}/\text{cm}^2$)	irradiation type	V_{bias} [V]
MPP1	July	0	–	150, 200
MPP2	July	0	–	150, 200
MPP3	October	0	–	150
MPP4	October	1	reactor neutrons	250, 350, 500, 550, 700
MPP5	October	1	25 MeV protons	500, 550
KEK1	October	0	–	100, 200
KEK2	October	0	–	100, 200

Table 1. Relevant quantities of the n-in-p samples.

each side. The samples MPP2 and MPP4 (see Table 1) have 15 guard-rings with a total inactive area of $610 \mu\text{m}$ on each side. In Figure 1 the two designs are illustrated. The inter-pixel isolation is achieved by means of a homogenous p-spray implantation.

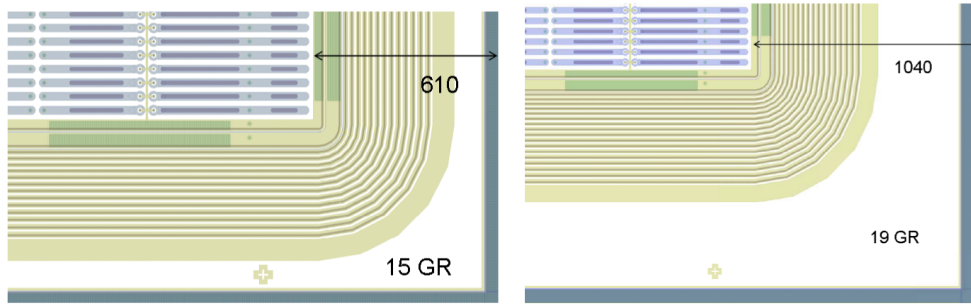


Figure 1. Left: View of a corner of an n-in-p sensor of the CiS production with 15 guard-rings. Right: View of a corner of an n-in-p sensor of the CiS production, with 19 guard-rings.

A BCB (Benzocyclobutene) coating has been applied to the pixelated side of the n-in-p pixel sensors, to prevent sparks between the area outside the guard ring area, that is at the same high potential as the back side, and the chip, at ground potential (Figure 2). The interconnection to the chips has been performed via bump-bonding at IZM-Berlin ³.

4.1.2 Beam test results

As documented in Table 1, during the first beam test period (July 2010) none of the CiS n-in-p sensors (namely MPP1, MPP2) were irradiated, while in the second period (October 2010) MPP4 was tested after irradiation with reactor neutrons [18] to a fluence of $1 \times 10^{15} \text{ n}_{eq}/\text{cm}^2$ and MPP5 was irradiated with low energy protons (25 MeV) at the cyclotron of the Karlsruhe Institute of Technology (KIT) [19] to the same equivalent fluence. MPP3 was kept as an unirradiated reference. In the following the performance of these five samples is presented.

Cluster size The cluster size distribution was studied for all sensors as a function of the bias voltage. A detailed breakdown is reported in Table 2. For the non-irradiated sample roughly 70 %

³Fraunhofer-Institut für Zuverlässigkeit und Mikrointegration, Berlin

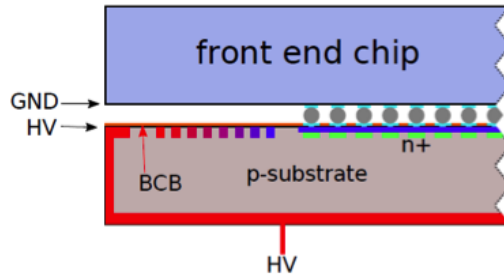


Figure 2. Schematics of a CiS n-in-p pixel assembly. The potential of the different parts is given. The BCB layer is indicated in orange.

of the cluster consisted of a single hit. Another 25 % are two-hit clusters, while the rest accounts for three and more hit clusters.

Due to trapping effects and lower overall charges for irradiated sensors one hit clusters are more often observed than in not irradiated samples. With increasing bias voltage the number of two hit clusters rises since it becomes more likely that a neighbouring pixel is above threshold as well. This behaviour can be clearly seen in Figure 3.

sample	V_{bias} [V]	CS=1 [%]	CS=2 [%]	CS=3 [%]	Charge sharing probability [%]
MPP1	150	65	31	2	33
MPP1	200	60	36	2	37
MPP2	200	75	23	1	24
MPP3	150	71	25	1	27
MPP4	250	95	4	1	4
MPP4	350	92	6	1	7
MPP4	500	88	9	1	10
MPP4	550	87	11	1	11
MPP4	700	85	13	1	14
MPP5	500	87	11	1	12
MPP5	550	78	19	1	21

Table 2. Cluster size (CS) composition for CiS modules measured at different bias voltages during beam tests; clusters were matched to a track. Charge sharing probability is reported too.

Collected charge The collected charge was measured as a function of the bias voltage for the different sensors. In Figure 4 the sub-pixel resolved charge collection profile is shown for MPP3 at V_{bias} of 150 V. The most prominent feature is the lower collected charge value on the right hand side, corresponding to the bias dot region where the pixel implant is connected to the bias grid. The same effect is evident in n-in-n devices with the same design (Section 5). Still also for this region the collected charge is well above the threshold.

Figure 5 shows lower collected charge along the edges of a pixel, due to charge sharing with the

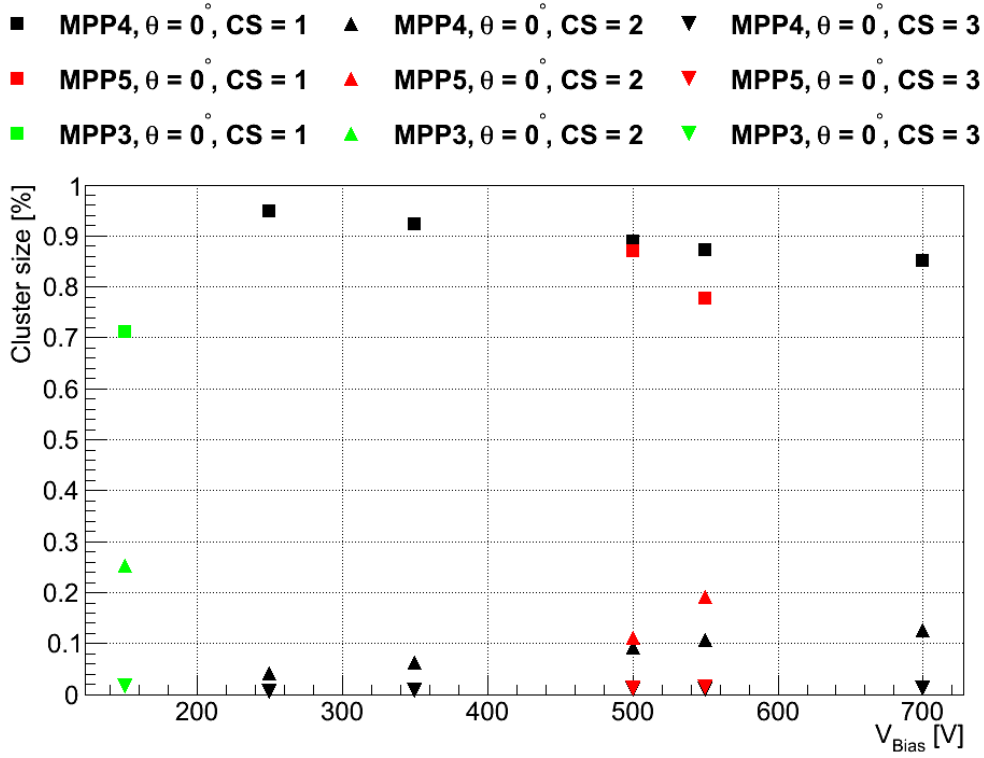


Figure 3. Relative cluster size abundance as a function of bias voltage for irradiated MPP4 and MPP5 devices. MPP3 (non-irradiated) are added for comparison. Particles were impinging at normal incidence. Errors on fractions are negligible and so not visible in the plot.

neighboring pixels. As charge sharing occurs, less charge is available for the pixel traversed by the particle, decreasing the probability to pass the electronics threshold. This effect is especially pronounced in the corners of the pixel, as charge can be shared among four pixels. Still in these regions deposited charges are high enough for an efficient operation of the device.

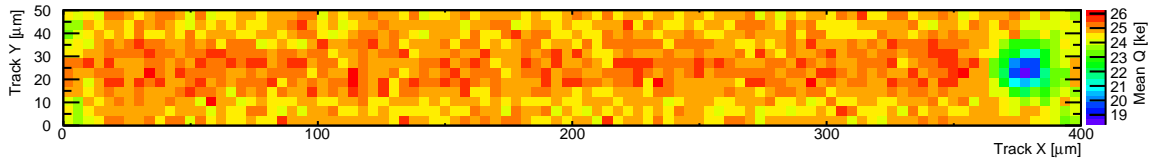


Figure 4. Charge collection within a single pixel by track position for MPP3 at V_{bias} of 150 V

Figure 6 shows the most probable charge for all samples. For comparison the charge collected by non-irradiated devices (MPP1 and MPP2) is included and a typical discriminator threshold of 3200 e is indicated. A systematic error on the collected charge of 400 e is assumed, due to the finite charge resolution of the ToT mechanism; a 5% systematic uncertainty is taken into account too, due to non-uniformities in the injection capacitances.

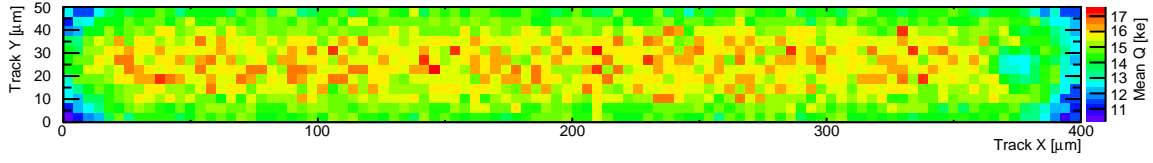


Figure 5. Charge collection within a single pixel by track position for MPP5 at $V_{\text{bias}} = 500$ V

274 Although the irradiated samples do not show saturation of the collected charge up to 700 V,
 275 already at low bias voltages the collected charge exceeds the electronics threshold by more than a
 276 factor of two and can thus be considered safe for tracking applications.

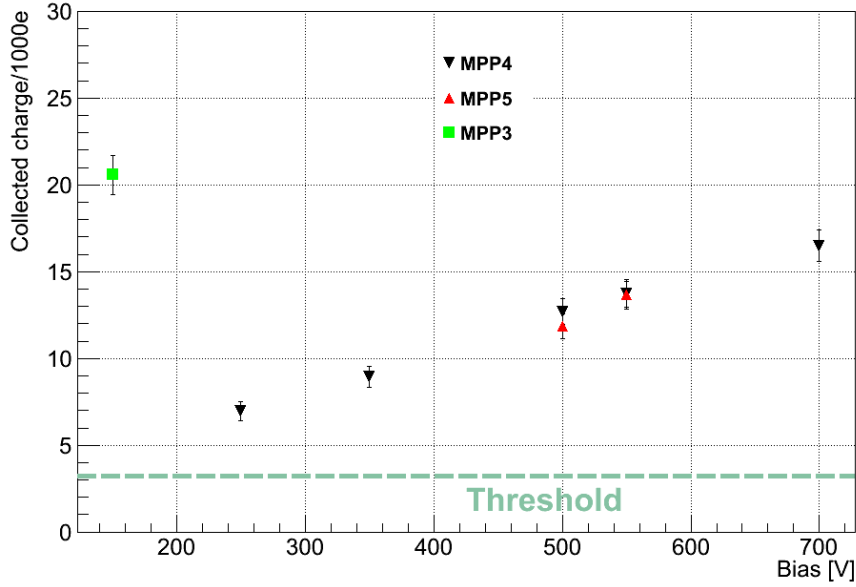


Figure 6. Charge collected in a cluster: most probable value of the charge distribution fitted to a Landau function convoluted with a gaussian as a function of the bias voltage. See text for the discussion on the assigned systematic uncertainty. The threshold value is also depicted as a dashed line.

277 **Charge sharing** In Figure 7 (top) the charge sharing probability within one pixel for MPP3 is
 278 shown. At normal track incidence increased charge collection probability is evident at the edges
 279 and corners of the pixel. The situation after irradiation is shown in Figure 7 (bottom). Here the
 280 charge sharing especially on the side of the punch through biasing is reduced, since there is a higher
 281 probability for the neighbouring pixel to be below threshold. This is also reflected in the average
 282 charge sharing probability given in Table 2 for the n-in-p CiS detectors in all states. With increasing
 283 bias voltage an increase of the charge sharing is observed for the irradiated sensors (MPP4, MPP5)
 284 due to the increase in the collected charge.

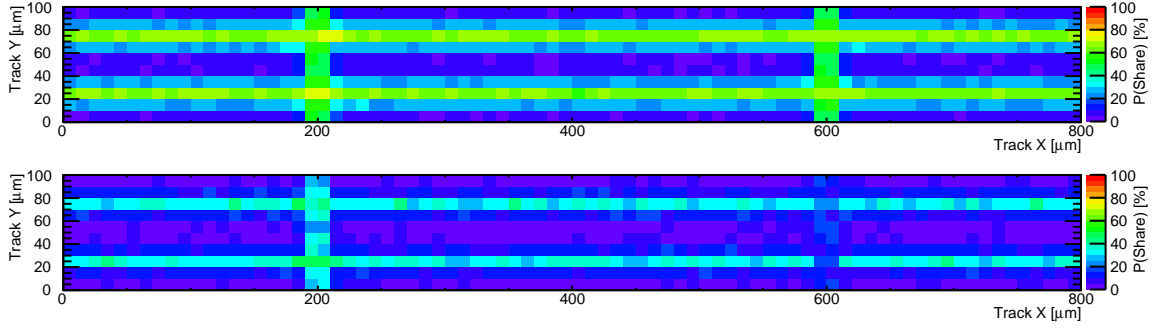


Figure 7. Charge sharing map for MPP3 detector, biased at 150 V (top) and for MPP4 detector, biased at 700 V.

Residuals Figure 8 shows the cluster position residual distribution for the irradiated module MPP5, biased at 500 V. The spatial resolution is compatible with the digital resolution, as one-hit clusters are dominant. For comparison, the residual distribution for MPP3 at 150 V is shown in Figure 9. No difference is appreciable between the two samples.

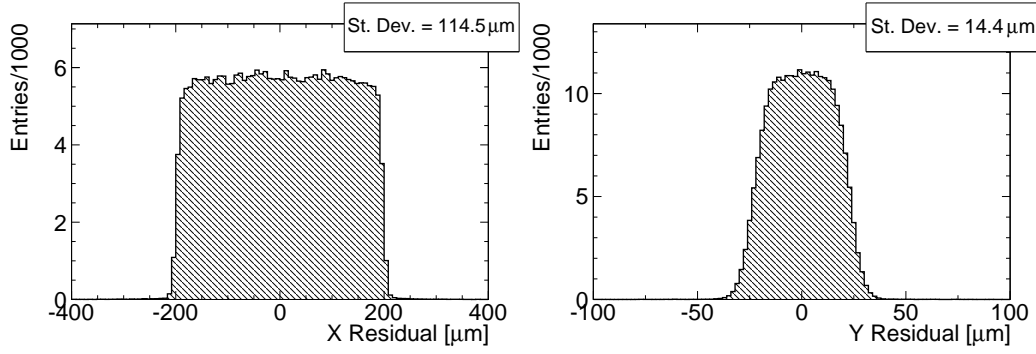


Figure 8. Residual distribution for irradiated sample MPP5 at V_{bias} of 500 V. Left: long pixel projection; right: short pixel projection.

For the irradiated assembly MPP5 Figure 10 shows in case of two hit clusters a resolution of $(7.2 \pm 2.5) \mu\text{m}$ in the core gaussian along the short pixel direction. For comparison, Figure 11 shows the two-hit cluster residuals for MPP3 at 150 V. After irradiation there are more noise related hits, clearly visible in Figure 10. The fitted core fraction indeed decreases with respect to unirradiated sample (Figure 11). Nonetheless, the tracking capabilities of irradiated DUTs, in terms of spatial resolution, are still satisfactory.

4.2 HPK sensors

In the following the p-type sensors produced at HPK will be introduced and their beam test results discussed.

4.2.1 Sensors design

Two modules with different sensor n-in-p layouts were beam tested, one with a polysilicon bias

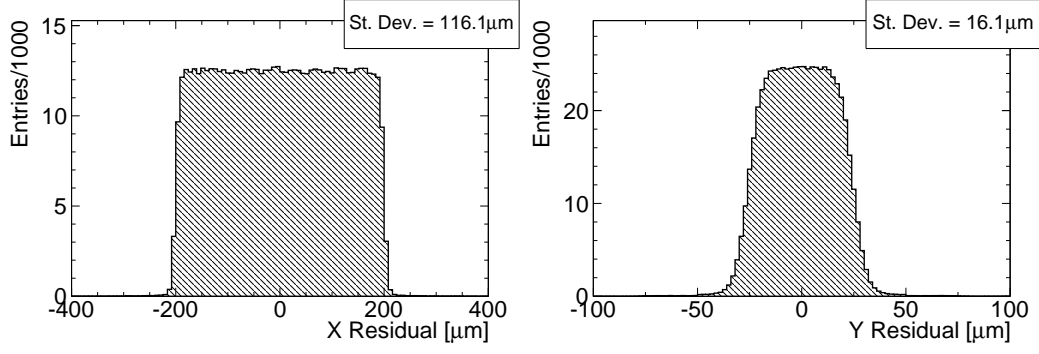


Figure 9. Residual distribution for non-irradiated MPP3 biased at 150 Volts. Left: long pixel projection; right: short pixel projection.

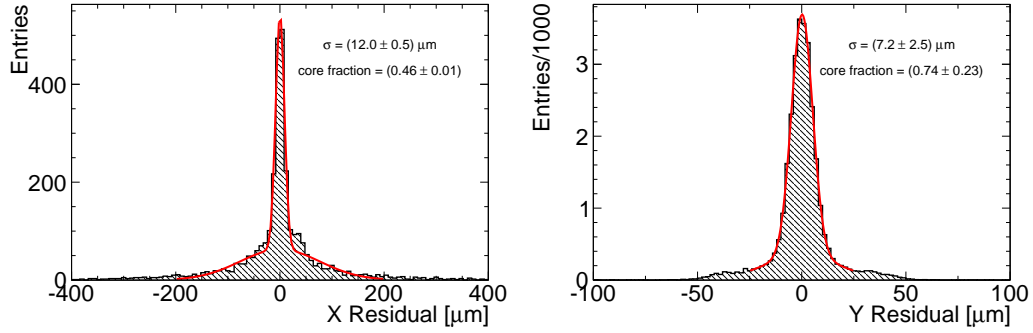


Figure 10. Residual distribution for irradiated sample MPP5 biased at V_{bias} of 500 V, for two-hit clusters. Left: long pixel projection; right: short pixel projection.

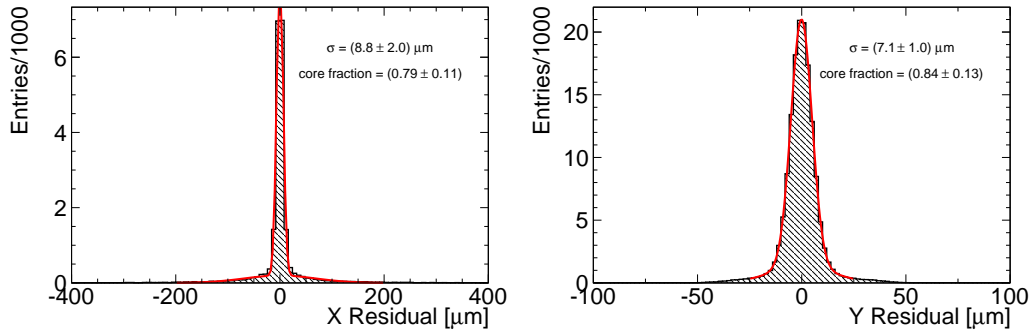


Figure 11. Residual distribution for unirradiated sample MPP3 at V_{bias} of 150 V, for two-hit clusters. Analysis restricted to clusters with 2 pixels. Left: long pixel projection; right: short pixel projection.

resistor and a common p-stop isolation (KEK1), and the other with a polysilicon bias resistor and an individual p-stop isolation (KEK2). Figure 12 shows a sketch of the pixel cell design for these two samples. A metal bias rail runs along each pixel double-column; there is no bias rail implant underneath it [22]. A parylene coating has been applied to the front side of the n-in-p pixel. These

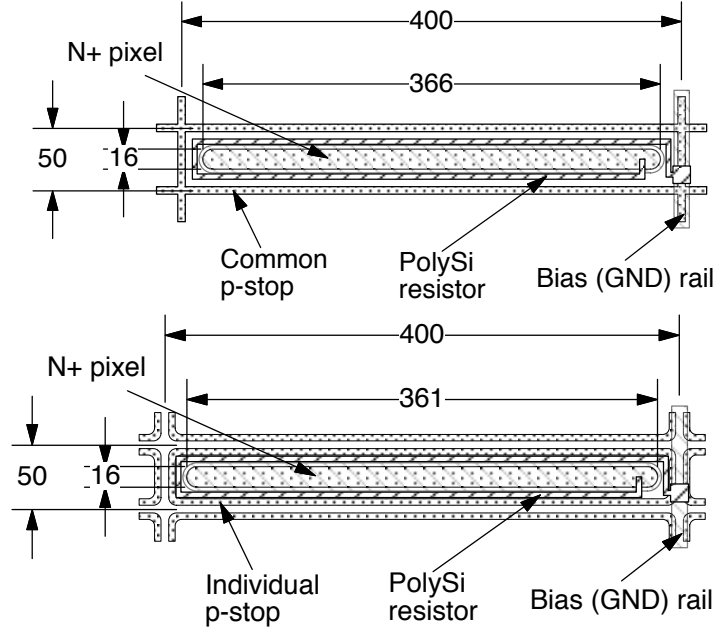


Figure 12. Pixel cell design details for KEK1 (top) and KEK2 (bottom) samples.

modules sensor is $320\ \mu\text{m}$ thick and the modules were tested before any irradiation.

4.2.2 Beam test results

The HPK samples characterization has been carried out by measuring cluster size, collected charge, charge sharing and spatial resolution as a function of the bias voltage.

Cluster Size The KEK1 and KEK2 samples were biased at 100 V and 200 V. The two samples perform in a similar way in terms of cluster size for particles at normal track incidence. As shown in table 3 (see also Figure 13) more than 80% of the clusters have just one hit pixel at 100 V bias voltage. As the bias voltage increases, the fraction of 2-pixel clusters increases as well, as more charge is collected and so the charge fluctuations are small compared to the threshold; this makes the probability of a pixel collecting a signal below threshold smaller.

sample	V_{bias} [V]	CS=1 [%]	CS=2 [%]	CS=3 [%]	Charge sharing probability [%]
KEK1	100	81	16	1	18
KEK1	200	73	23	2	26
KEK2	100	83	14	1	16
KEK2	200	76	20	2	22

Table 3. Cluster composition for HPK detectors for different bias voltages; charge sharing probability is reported in the last column. Clusters were matched to a track.

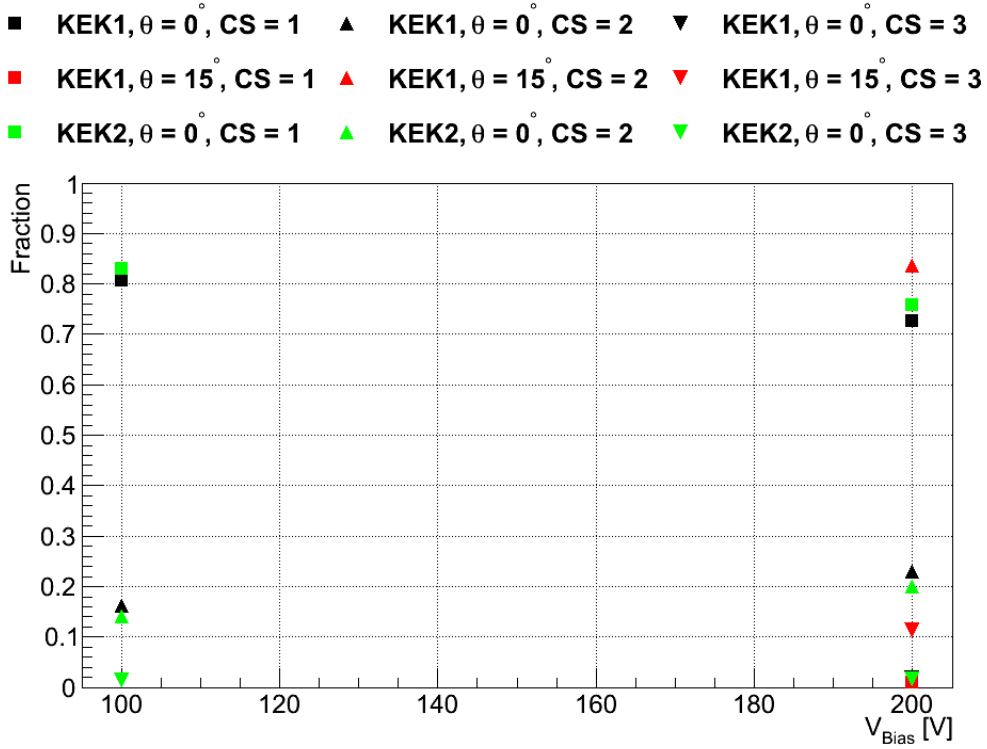


Figure 13. Fraction of cluster sizes as function of the bias voltage for HPK samples; particles were impinging at different angles too.

Collected charge In Figure 14 the collected charge per cluster is shown as a function of bias voltage for the KEK sensors. The charge collection improves with bias voltage, but already at 100 V the signal is more than 4 times the threshold. At 200 V the expected full charge is collected.

Charge sharing Figure 15 shows the charge sharing map for KEK1. At normal incidence the fraction of charge sharing is more than 25 % for a sensor biased at 200 V. Results for KEK2 show that the charge sharing is less effective (22 %): this can be related to the different layout between the two sensors. In the bottom figure the combined effect of the bias metal rail and the individual p-stop is visible. Results are summarized in table 3.

Residuals Figure 16 shows the residual distribution for all clusters at normal track incidence. The spatial resolution is about $16 \mu\text{m}$ along the short pixel direction, which is comparable with the digital resolution of $\text{pitch}/\sqrt{12}$; the same is true for the long pixel direction (RMS about $116 \mu\text{m}$). No difference is noticeable between KEK1 and KEK2 sensors.

Figure 17 shows the residual distribution for two-hit clusters. For these, the spatial resolution is found to be around $7 \mu\text{m}$ in the short pixel direction and around $9 \mu\text{m}$ for the long one (see also Table 4). The spatial resolution when the cluster contains two hits is larger than the telescope pointing-resolution and gives an estimate of the charge sharing region between neighbouring pixels.

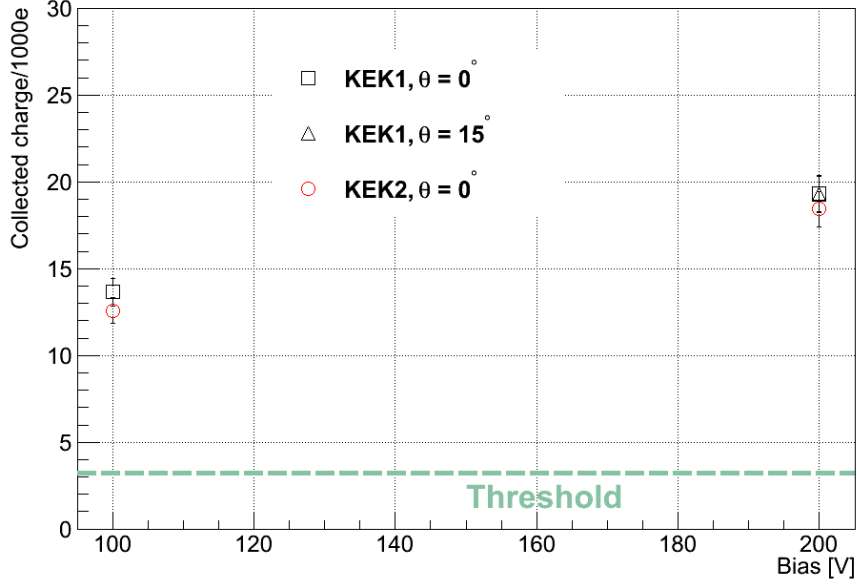


Figure 14. Collected charge as a function of the bias voltage for HPK samples; particles were impinging at different angles too. A threshold of 3200 e is indicated.

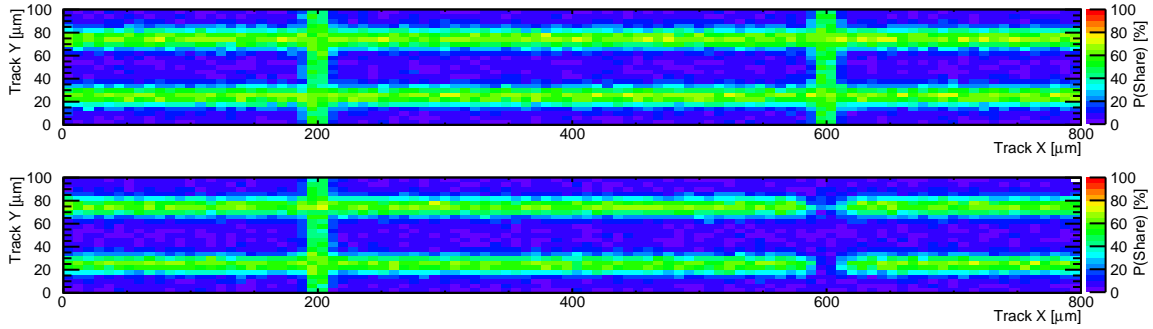


Figure 15. Charge sharing map for KEK1 (top) and KEK2 (bottom) at V_{bias} of 200 V.

5. Radiation hardness of n-in-n sensors

The n-in-n sensor technology used in the current ATLAS Pixel detector have been tested to fluences up to $1.1 \times 10^{15} \text{ n}_{eq}/\text{cm}^2$ [11]. To evaluate the usability of n-type bulk material for IBL and future detector upgrades, sensors have been irradiated with fluences as high as $2 \times 10^{16} \text{ n}_{eq}/\text{cm}^2$ using both reactor neutrons (Jožef-Stefan Institute, Ljubljana) [18] and protons of 25 MeV (Karlsruhe Institute of Technology - KIT) [19] or 24 GeV (CERN) [12].

Most of the sensors follow the ATLAS Pixel detector sensor design with 16 guard rings and a thickness of $250 \mu\text{m}$. DO6 is a special sensor with only 11 guard rings overlapping the pixel region,

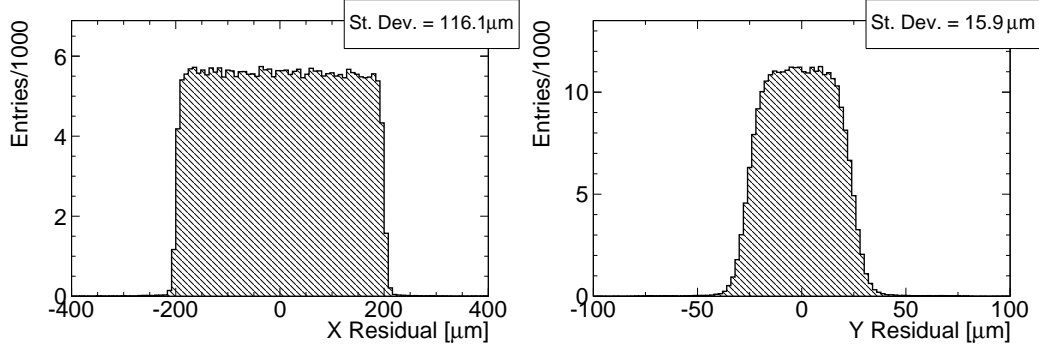


Figure 16. Cluster position residual distribution for non-irradiated sample KEK1 at V_{bias} of 200 V at normal incidence. Left: long pixel projection; right: short pixel projection.

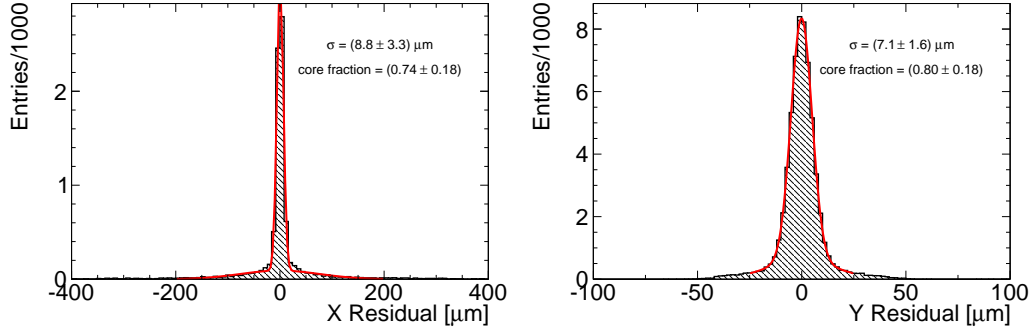


Figure 17. Residual distribution for non-irradiated KEK1 biased at 200 Volts clusters with 2 pixels. Left: long pixel projection; right: short pixel projection.

Sample	V_{bias} [V]	pitch (μm)	RMS (μm)	core σ (μm)	core fraction [%]
KEK1	100	400	116.00 ± 0.14	9.00 ± 0.13	68
KEK2	100	400	115.00 ± 0.14	9.40 ± 0.20	53
KEK1	200	400	116.10 ± 0.20	9.0 ± 3	74
KEK2	200	400	115.00 ± 0.15	9.31 ± 0.18	60
KEK1	100	50	16.000 ± 0.020	7.14 ± 0.06	78
KEK2	100	50	15.800 ± 0.020	6.88 ± 0.05	78
KEK1	200	50	15.90 ± 0.05	7.1 ± 1.6	80
KEK2	200	50	16.000 ± 0.021	6.81 ± 0.05	79

Table 4. Summary of residual results for KEK1 and KEK2 samples. Core σ and fraction are evaluated for 2-pixels clusters only.

338 designed to study possibilities to reduce the inactive area at the edge of the sensor (see section 6)
 339 and produced on 285 μm thick bulk material. The n-type sensors were produced at CiS.

340

A total of 5 irradiated n-in-n pixel sensors were tested. Table 5 gives a summary of the fluences the sensors were irradiated to. See also [16].

name	thickness (μm)	fluence ($10^{15} \text{ n}_{\text{eq}}/\text{cm}^2$)	irradiation type
DO6	285	0	–
DO7	250	1	protons (KIT)
DO8	250	1	reactor neutrons
DO9	250	5	reactor neutrons
DO10	250	20	reactor neutrons

Table 5. Summary of irradiated n-in-n samples in the testbeams. KIT stands for 25 MeV energy proton irradiation.

5.1 Results

Charge collection One of the main effects of irradiation is the increased trapping, which leads to a reduced signal amplitude. As the trapping probability depends on the charge carrier velocity, the collected charge was measured as a function of the bias voltage. Figure 18 shows the results for all irradiated n-in-n samples in the two beam test periods; see Table 5 too. A systematic error on the collected charge of 400 e is assumed, due to the finite charge resolution of the ToT mechanism; a 5% systematic uncertainty is taken into account too, due to non-uniformities in the injection capacitances.

After $5 \times 10^{15} \text{ n}_{\text{eq}}/\text{cm}^2$, the collected charge still exceeds 10 ke at a bias voltage of 1000 V. Even if the collected charge is shared equally between two neighboring pixels, this charge is sufficient to detect the hit with FE-I3.

Figure 19 top, shows that charge is predominantly lost in the region of the punch-through bias grid system. At very high fluences ($2 \times 10^{16} \text{ n}_{\text{eq}}/\text{cm}^2$, DO10 sample) an impact on the sensor behaviour in the region of the bias grid cannot be determined by using the charge collection method (Figure 19, bottom).

Charge sharing Figure 20 shows the charge sharing probability for DO9 at a bias voltage of 1200 V. Reduced charge sharing probability is visible in the region of the bias dot and the bias grid network.⁴ Less charge is deposited here, so the probability for the second pixel in a 2-pixel cluster to be below threshold is higher. As only the bias trace makes the difference between both pixel sides, it might cause the lower charge sharing probability. Furthermore, one can see that the region of the bias dot is not effected.

While for DO9 a clear increase in charge sharing probability towards the edges of the pixel is visible, at higher fluence the collected charge becomes too small for any significant charge sharing to be observable. This can also be seen in the fractions of clusters with 1, 2, and more pixels. Figure 21 shows the fractions of 1-pixel, 2-pixel, and larger clusters as a function of the bias voltage; see Table 5 too. It is evident, that with increasing bias voltage the cluster size increases, due to the

⁴The bias grid network is an aluminum trace arranged on top of the intermediate pixel region connecting all bias dots.

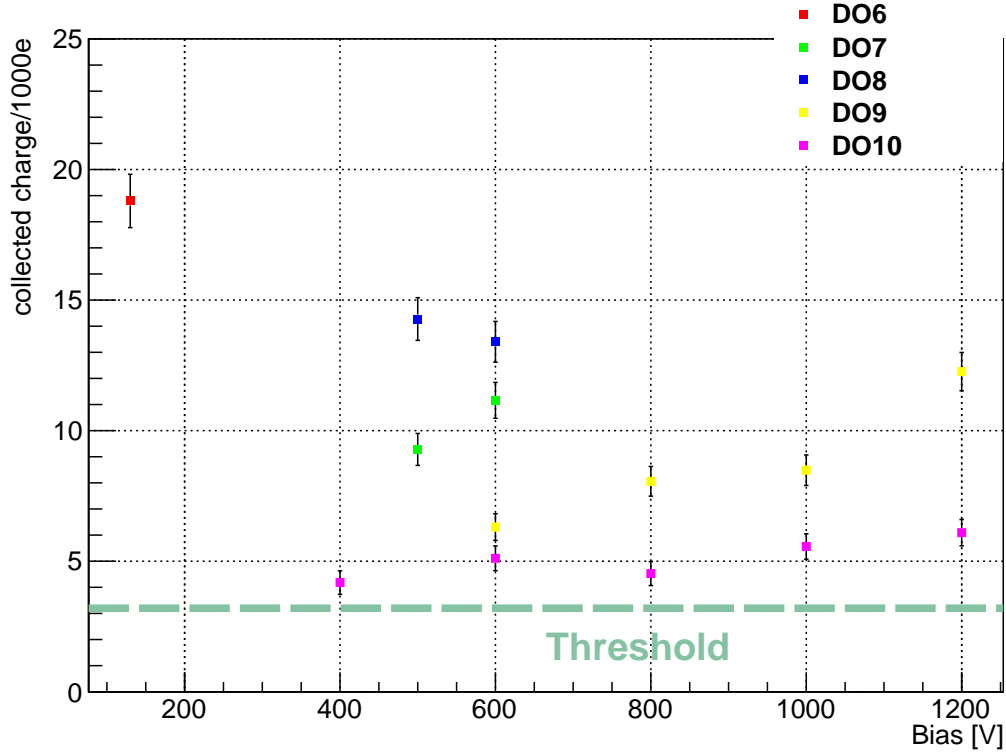


Figure 18. Collected charge as a function of bias voltage for n-in-n samples irradiated to different fluences (see details in the text). A threshold of 3200 e is indicated.

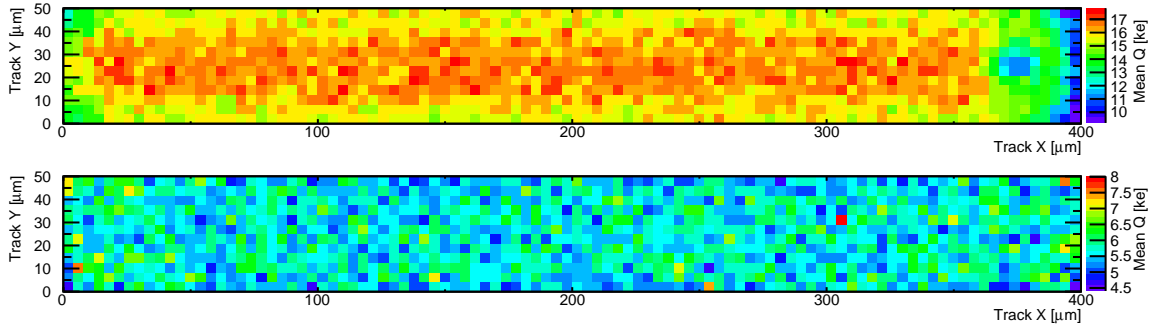


Figure 19. Charge collection within a pixel. Top: DO9 at $V_{bias}=1200$ V. Bottom: DO10 at $V_{bias}=1000$ V.

369 reduced trapping. At a given voltage the fraction of 1-pixel clusters increases with fluence, as more
 370 charge is lost due to trapping.

371 For samples irradiated up to $5 \times 10^{15} \text{ n}_{eq}/\text{cm}^2$ the cluster size increases slightly with bias voltage,
 372 while at $2 \times 10^{16} \text{ n}_{eq}/\text{cm}^2$ the fraction of clusters with 2 or more hit pixels is very small and stays
 373 nearly constant over the accessible voltage range.

374 Plotting the residual distribution for 2-pixel clusters only allows to determine the width of the

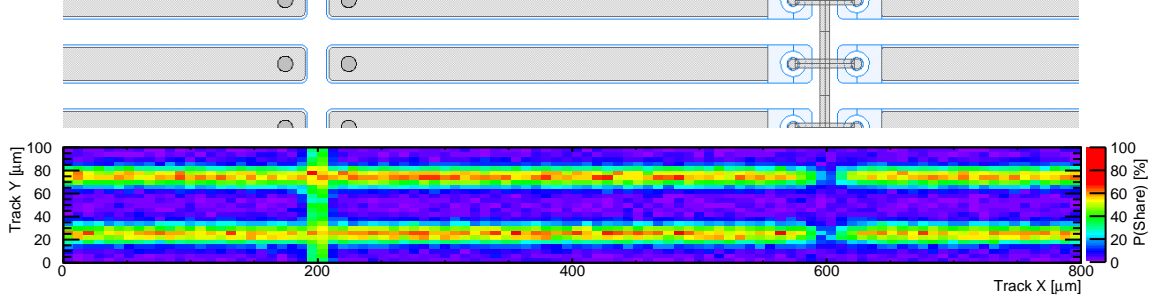


Figure 20. Top: Design of the sample of the region shown in the plot below. Bottom: Charge sharing probability for DO9 at $V_{bias}=1200V$. Note the reduced charge sharing in the bias grid region on the right-hand side of the central pixel.

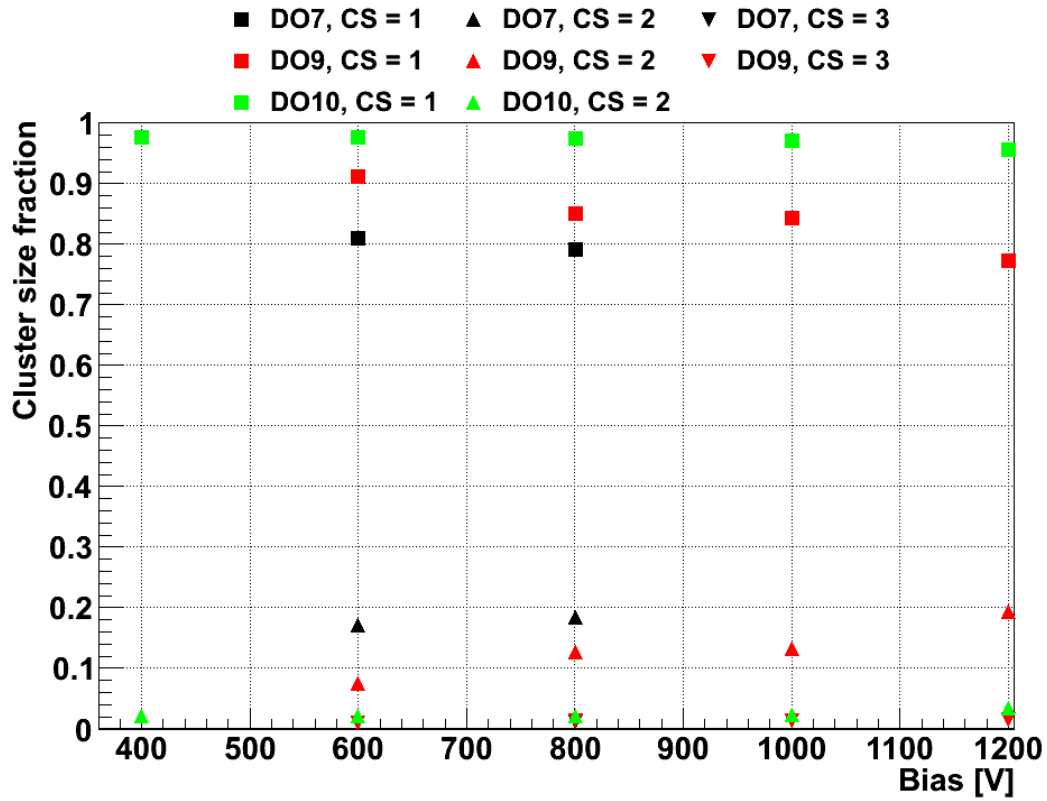


Figure 21. Fractions of 1-, 2-, and 3-hit clusters as function of bias voltage for irradiated n-in-n samples; see text for details. Error bars are too small to be visible.

region between pixels, where charge sharing occurs. Figure 22 shows the distributions for DO9 ($5 \times 10^{15} \text{ n}_{eq}/\text{cm}^2$) and DO10 ($2 \times 10^{16} \text{ n}_{eq}/\text{cm}^2$). After correcting for the telescope resolution, the widths of the charge sharing regions are $7.1 \mu\text{m}$ and $7.7 \mu\text{m}$. These values correspond very well with the width found for an unirradiated sample of $6.4 \mu\text{m}$. This indicates that the lateral diffusion of the charge cloud does not change significantly with irradiation.

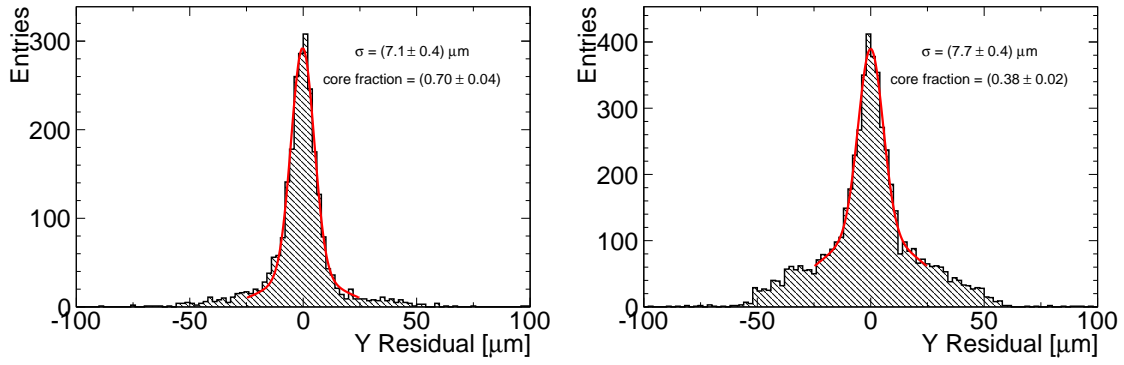


Figure 22. Residual distributions for 2-pixel clusters only. Shown are distributions samples irradiated to $5 \times 10^{15} \text{ n}_{\text{eq}}/\text{cm}^2$ (left: DO9, bias voltage 1000 V) and $2 \times 10^{16} \text{ n}_{\text{eq}}/\text{cm}^2$ (right, DO10, bias voltage 1200 V), respectively.

Residuals Figure 23 shows the residual distributions in the $50 \mu\text{m}$ pixel direction for the unirradiated sample (DO6) and the sample irradiated to $2 \times 10^{16} \text{ n}_{\text{eq}}/\text{cm}^2$, respectively. The widths of the distributions are $16 \mu\text{m}$ and $15.4 \mu\text{m}$, comparable with the expected digital resolution of $14.4 \mu\text{m}$. Thus, no influence of radiation damage on the spatial resolution can be observed.

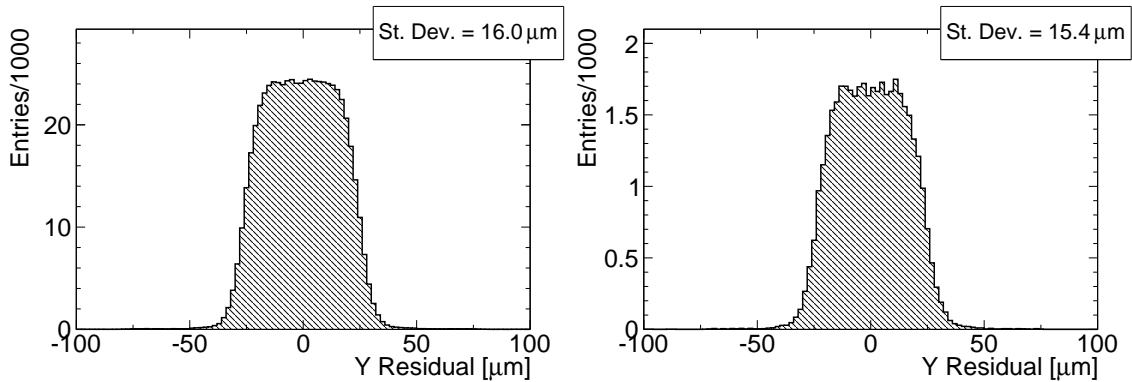


Figure 23. Residual distributions in the short pixel direction for an unirradiated sample (DO6, left) and a sample irradiated to $2 \times 10^{16} \text{ n}_{\text{eq}}/\text{cm}^2$ operated at a bias voltage of 1000 V (DO10, right). No deterioration of the spatial distribution with irradiation is visible.

6. Slim Edge

For slim edge studies the outermost pixels of a sample are of special interest. Therefore, the samples were mounted such that the edge of the sensor was well within the trigger acceptance window. Special analysis classes were written to investigate the characteristics of the edge pixels. The basic principle is the same as for the charge collection analysis but instead of overlaying all pixels onto one single pixels only pixels at the sensor edge are used and the special geometry is conserved in the overlay process.

391 For the IBL sensors the width of the inactive region at the edge of each sensor tile has to be
 392 reduced significantly with respect to the roughly about 1 mm on each side of the current ATLAS
 393 Pixel detector sensors. One approach is to shift the guard-rings on the p^+ -side inwards. Two
 394 specially designed DUTs were tested to study the impact of an overlap between the active pixel
 395 region with the guard ring region, where the electric field in the sensor is not homogenous.
 396 In the DO6 sample, the overlap between active pixel region and guard ring region is $210\text{ }\mu\text{m}$, with
 397 the number of guard rings reduced to 11. In the DO3 sample groups of 10 pixels are shifted towards
 398 the edge of the sensor in steps of $25\text{ }\mu\text{m}$, increasing the area in which the pixels overlap with the
 399 guard-rings (see Figure 24).

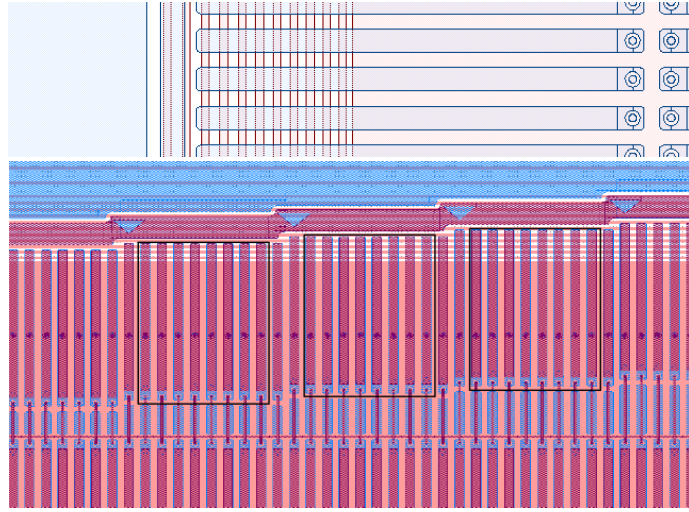


Figure 24. Test structures for slim edge studies. Top: DO6, the active pixel region overlaps the guard rings by $210\text{ }\mu\text{m}$. Bottom: DO3, groups of 10 pixels shifted towards the edge of the sensor in steps of $25\text{ }\mu\text{m}$.

400 The test structures were mounted such that the edge of the sensor was well in the center of the
 401 trigger window, allowing to study charge collection in the shifted pixels in some detail. Figure 25
 402 shows the collected charge in the overlap region of DO6. With increasing distance from the bias
 403 voltage pad the collected charge decreases, due to the inhomogeneously formed depletion zone. It
 404 is evident that the collected charge is sufficient to ensure good hit efficiency up to about $200\text{ }\mu\text{m}$
 405 from the edge of the bias voltage pad.
 406

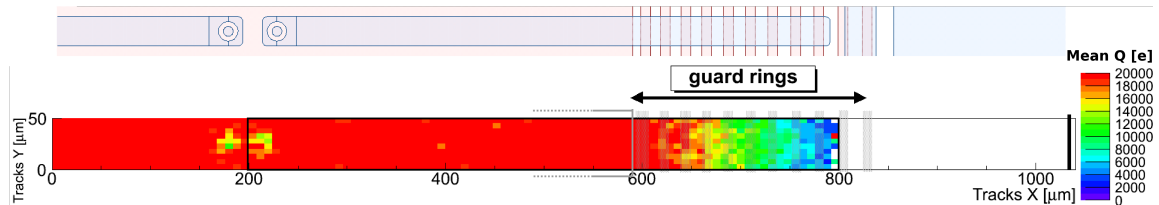


Figure 25. Charge collection in the pixels shifted underneath the guard rings.

Figure 26 shows the collected charge in the overlap region for the DO3 sample. Data from pixels with the same shift with respect to the edge of the bias voltage pad is plotted into one pixel. The drop in collected charge systematically occurs at the same distance from the bias voltage pad, regardless of the shift of the pixel. This indicates, that the loss of collected charge is indeed due to the depletion zone which is expected to be inhomogeneous along the x-axis (orthogonal to the bias voltage pad) but homogeneous along the y-axis (parallel to the bias voltage pad). Further studies of this kind can be found in [32].

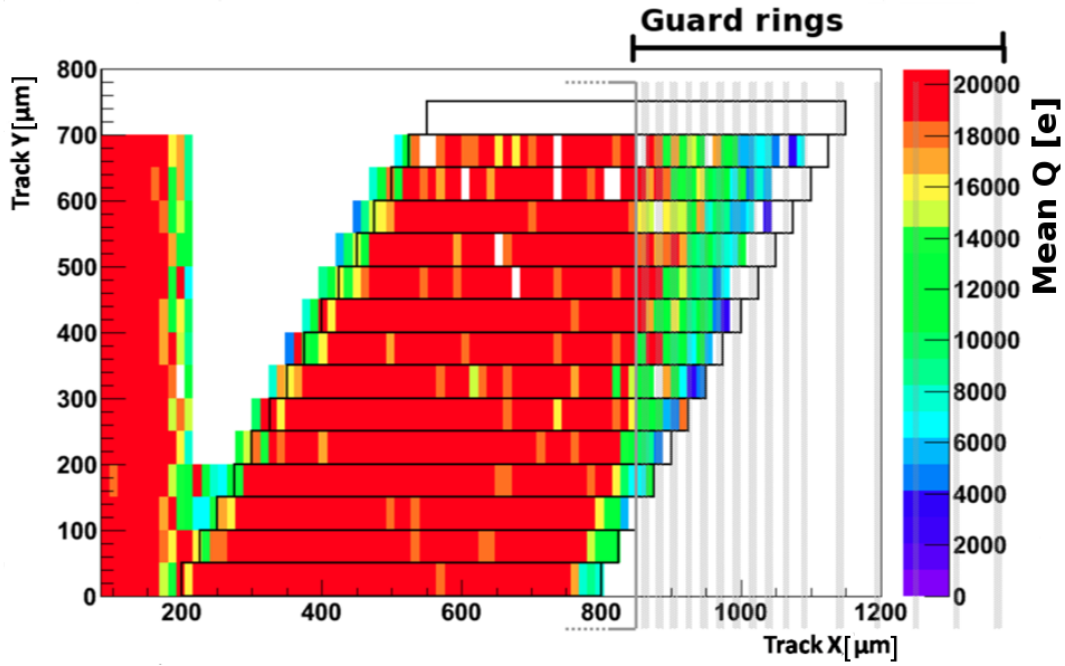


Figure 26. Charge collection in the pixels shifted underneath the guard rings.

7. Conclusion

Planar silicon sensors have been tested in high energy pion beams at the CERN SPS North Area in 2010 by the ATLAS Planar Pixel Sensors (PPS) collaboration.

The goals of the measurement program were threefold: demonstrate the suitability of p-bulk sensors for tracking purpose, prove the radiation hardness of n-bulk sensors and realize pixel sensors with reduced inactive edge area.

Pixelated p-bulk sensors produced by several vendors were tested to evaluate their performance before and after irradiation. In terms of collected charge, charge sharing, and spatial resolution the

422 performance of the p-bulk sensors was very good and comparable to that of n-bulk sensors. The
423 issue of the high potential on the pixelated side of the sensor was tested and operation of the sensors
424 was proven to be very stable.

425 The radiation hardness of n-bulk sensors was tested up to unprecedented fluences, with a
426 maximum of $20 \times 10^{15} n_{eq} cm^{-2}$. At a bias voltage of 1.2 kV a collected charge of about 6 ke,
427 which is sufficient to guarantee reasonable hit efficiency. Despite the rather small collected charge
428 and the reduced charge sharing between pixels, no significant deterioration of the spatial resolution
429 was observed.

430 In order to reduce the inactive area at the edge of n-bulk sensors, several modified sensor
431 layouts were tested to study the influence of a reduction of the number of guard rings and an
432 increasing overlap between the active pixel region and the guard ring region on the backside of
433 the sensor. It was found that charge collection efficiency reduces with increasing distance from
434 the edge of the bias voltage pad due to the in-homogeneously formed depletion zone in the sensor.
435 However, the collected charge is sufficient for reliable particle detection up to a distance of about
436 $200 \mu m$ from the bias voltage pad. This was very encouraging for the planar ATLAS IBL candidate
437 design, which was finally designed employing the measures tested in the beam test measurements
438 described in this paper.

Acknowledgements

The authors would like to express their gratitude both to V. Cindro, G. Kramberger, I. Mandić for their valuable support with irradiations at the TRIGA reactor of the Jožef Stefan Institute, Ljubljana, to A. Dierlamm for his help at the Irradiation Center, Karlsruhe, and to M. Glaser for his help at the CERN PS irradiation facility.

The work has been partially performed in the framework of the CERN RD50 Collaboration. This work is supported by the Commission of the European Communities under the 6th Framework Programme “Structuring the European Research Area”, contract number RII3-026126.

We gratefully acknowledge the financial support of the German Federal Ministry of Science and Education (BMBF) within their excellence program, in particular as part of the collaborative research center “FSP 101-ATLAS, Physics on the TeV-scale at the Large Hadron Collider”.

We acknowledge the support of the Initiative and Networking Fund of the Helmholtz Association, contract HA-101 (“Physics at the Terascale”).

References

- [1] *ATLAS Pixel Detector Electronics and Sensors*,
The ATLAS collaboration, JINST 3 P07007, 2008
- [2] *ATLAS Insertable B-Layer Technical Design Report*,
ATLAS TDR 19, CERN/LHCC 2010-013,
<http://cdsweb.cern.ch/record/1291633/files/ATLAS-TDR-019.pdf>
- [3] *LHC near and medium term prospect*,
M. Lamont, <http://dx.doi.org/10.3204/DESY-PROC-2010-01/8>
- [4] *Stragglings in thin silicon detectors*,
H. Bichsel, Rev. Mod. Phys. **60** 663 (1988)
- [5] *Diamond pixel modules*,
D. Asner *et al*, Nucl. Instr. Meth. **A636**, 125 - 129 (2011).
- [6] *3D silicon pixel sensors: Recent test beam results*,
P. Hansson *et al.*, Nucl. Instr. Meth. **A628**, 216 - 220 (2011).
- [7] ATLAS Upgrade Planar Pixel Sensor R&D Project,
see also <https://edms.cern.ch/document/966140>
- [8] *Results from the EUDET telescope with high resolution planes*,
A. Bulgheroni *et al.*, Nucl. Instr. Meth. **A623**, 399-401 (2010).
- [9] *The FEI3 readout chip for the ATLAS pixel detector*,
I. Perić *et al.*, Nucl. Instr. and Meth. **A565** 178 - 187 (2006).
- [10] TurboDAQ
- [11] *Test beam performance of the ATLAS Pixel Detector modules*,
A. Andreazza on behalf of the ATLAS Pixel Collaboration, Nucl. Instr. Meth. **A565**, 23 - 29 (2006).
- [12] *New irradiation zones at the CERN-PS*,
M. Glaser *et al.*, Nucl. Instr. Meth. **A426**, 72 - 77 (1999).

- 477 [13] *Spatial resolution of silicon microstrip detectors*,
478 R. Turchetta Nucl. Instr. Meth. **A335**, 44 - 58 (1993).
- 479 [14] *Highly segmented thin microstrip detector with data-driven fast readout*,
480 M. Bomben *et al.*, Nucl. Instr. Meth. **A623** 159-161 (2010).
- 481 [15] *Design studies on sensors for the ATLAS Pixel Detector*,
482 F. Hügging, Nucl. Instr. Meth. **A477** 143-149 (2002).
- 483 [16] *Radiation hardness studies of n^+ -in- n planar pixel sensors for the ATLAS upgrades*,
484 S. Altenheiner *et al.*, Nucl. Instr. Meth. **A658**, 25 - 29 (2011).
- 485 [17] *Development and operation of a testbeam setup for qualification studies of ATLAS pixel sensors*,
486 G. Troska, Ph. D. Thesis, TU Dortmund, 2012
- 487 [18] *Analysis of neutron flux distribution for the validation of computational methods for the optimization
488 of research reactor utilization*,
489 L. Snoj *et al.*, Appl. Rad. and Iso. **69** (2011) 136
- 490 [19] Irradiation Center of Karlsruhe Institute of Technology (KIT)
- 491 [20] *Characterization and performance of silicon n-in-p pixel detectors for the ATLAS upgrades*,
492 P. Weigell *et al.*, Nucl. Instr. and Meth. **A658** 36 - 40 (2011).
- 493 [21] *Measurements of spatial resolution of ATLAS pixel detectors*,
494 T. Lari *et al.*, Nucl. Instr. and Meth. **A465** 112 - 114 (2001).
- 495 [22] *Development of n-in-p silicon planar pixel sensors and flip-chip modules for very high radiation
496 environments*,
497 Y. Unno *et al.*, Nucl. Instr. and Meth. A **650** (2011), p. 129
- 498 [23] *Test Beam Measurements with the EUDET Pixel Telescope*,
499 J. Behr, <http://www.eudet.org>, EUDET-Report-2010-01
- 500 [24] *A Trigger/Timing Logic Unit for ILC Test-beams*,
501 D. Cussans, Contribution to “TWEPP-07 Topical Workshop on Electronics for Particle Physics”,
502 3-7 September 2007, Prague (Czech Republic)
- 503 [25] *A ten thousand frames per second readout MAPS for the EUDET beam telescope*,
504 C. Hu-Guo, CERN-2009-008
- 505 [26] *Jets at High Q^2 at HERA and Test Beam Measurements with EUDET Pixel Telescope*,
506 J. Behr, Dissertation & Ph. D. thesis (2010) - ZEUS, Universität Hamburg, Chapter 16
- 507 [27] *MILLIPEDE*,
508 V. Blobel, <http://www.desy.de/~blobel>
- 509 [28] *Full simulation of a testbeam experiment including modeling of the Bonn Atlas Telescope and Atlas
510 3D pixel silicon sensors*,
511 K. N. Sjøbæk, Thesis presented for the Master of Science degree in Experimental Particle Physics,
512 Department of Physics, University of Oslo, Appendix C
- 513 [29] *The Deterministic Annealing Filter*,
514 S. Fleischmann, CERN-THESIS-2007-011, pp.19 - 23
- 515 [30] *Notes on the fluence normalisation based on the NIEL scaling hypothesis*,
516 The ROSE Collaboration, Technical Note ROSE/TN/2000-02, CERN

- 517 [31] <http://root.cern.ch>
- 518 [32] *Planar slim-edge pixel sensors for the ATLAS upgrades,*
- 519 T. Wittig *et al*, 2012_JINST_7_C02051